Geodetic Evidence for Distributed Flow Below the Brittle Crust of the Walker Lane, Western United States

Nina M. Miller[1], Corné Kreemer[1,2], William C. Hammond[1], Geoffrey Blewitt[1]

[1]Nevada Geodetic Laboratory, Nevada Bureau of Mines And Geology, University of Nevada, Reno
[2]Nevada Seismological Laboratory, University of Nevada, Reno

Key Points:

- Geodetic velocities in the Walker Lane (WL) reflect distributed shear in the lower crust rather than deformation due to discrete faults.
- The width of and velocity across the northern WL is 172±6 km and 7.2±0.3 mm/yr, resp., and 116±4 km and 10.1±0.2 mm/yr for the central WL.
- Estimating fault slip rates using models that assume their downdip continuation into the lower crust may be inappropriate for some regions.

Corresponding author: Nina Miller, `ninamiller@unr.edu`

Abstract

The predominant approach for modeling faults in the Earth's crust represents them as elastic dislocations, extending downdip into the lower crust, where the faults slip continuously. The resulting surface deformation features strain accumulation concentrated across locked faults during the interseismic period. An alternative model proposes faults confined to the elastic crust, with surface deformation driven by a wide zone of distributed shear underneath. Using high-precision GPS data, we analyze deformation profiles across the Walker Lane (WL), USA. The WL is a transtensional region of complex faulting, which delineates the western edge of the Basin and Range province and accommodates a significant portion of the Pacific-North American plate boundary deformation budget. Despite a dense geodetic network surveyed collectively for nearly 20 years, horizontal velocities reveal no evidence of localized strain rate accumulation across fault surface expressions. Instead, deformation within the shear zone is uniformly linear, suggesting that the surface velocities reflect distributed shear within the ductile crust rather than discrete fault deformation. This implies no downdip fault extension below the seismogenic layer. The shear zone, bound by the Sierra Nevada crest in the west, is 172±6 km wide in the northernmost WL narrowing to 116±4 km in the central WL. This study's conclusion challenges the assumption of the presence of dislocations in the lower crust when estimating geodetic slip rates, suggesting that slip rates are instead controlled by the fault's position and orientation within the shear zone. This has important implications for quantifying seismic hazards in regions with complex fault systems.

Plain Language Summary

Interpreting Earth's surface deformation, measured by high-precision GPS stations, is crucial for understanding plate tectonics and assessing seismic hazard. Traditionally, the assumption has been that faults in the Earth's upper crust extend as discrete dislocations into the lower crust. In this paper, we show that there is no compelling evidence of this in the Walker Lane region of California and Nevada. Instead, we conclude that the geodetically measured deformation on the surface reflects uniform shearing in the lower crust. Our findings support the interpretation of the Walker Lane region as a developing large-scale strike-slip fault and imply that the current method of estimating slip rates on the faults may be inappropriate.

1 Introduction

A long-standing concept in tectonic geodesy is that of an elastic dislocation model (EDM), in which a fault is represented as a locked dislocation in the upper crust and with a continuously creeping continuation into the viscoelastic lower crust. For vertical faults, the EDM predicts an arctangent shape of the horizontal surface velocity field (Savage & Burford, 1973), resulting in localized shear strain on the surface across the fault trace. These signals can be detected in investigations of active crustal deformation, accessible through geodetic techniques such as InSAR (e.g. Wright et al., 2001; Tong et al., 2013; Cakir et al., 2014; Chaussard et al., 2016; Weiss et al., 2020), GNSS networks (e.g. Wdowinski et al., 2004; Meade & Hager, 2005; Schmalzle et al., 2006; Vernant, 2015; Hussain et al., 2018), alignment and leveling arrays (e.g. Savage et al., 1979; Galehouse & Lienkaemper, 2003; Mongovin & Philibosian, 2021).

A viscoelastic dislocation model (VEDM) assumes the same structure as the EDM, but takes the coupling between the viscous and the elastic layers into account (Savage & Prescott, 1978; Savage & Lisowski, 1998; Savage, 2000; Pollitz et al., 2008). The implication of VEDM is time-dependent strain rates, with a flattening of the arctangent shape late in the fault's seismic cycle.

A competing concept is that of the shear zone model (SZM) (Prescott & Nur, 1981; Bourne et al., 1998; Pollitz, 2001), in which faults only exist in the elastic part of the crust, with the ductile layer underneath deforming smoothly without discrete dislocations. In this model, the surface velocity pattern is mostly linear (i.e., constant shear strain rate), reflecting the underlying shear. The elastic layer acts as a smoothing filter, broadening the expression of the shear zone and making the surface deformation more distributed with increasing thickness of the elastic layer.

The EDM has gained popularity, in part, due to its simplicity and utility in the estimation of slip rates on the faults (e.g. Fay & Humphreys, 2005; Schmalzle et al., 2006; Hill & Blewitt, 2006). The deformation across large-scale strike-slip faults generally exhibits the arctangent shape and is fit well by the EDM or by the VEDM (Chuang & Johnson, 2011; Vernant, 2015; Y. Zhu et al., 2020). Studies of exhumed peridotite massifs, ophiolites, and xenoliths (e.g. Norris & Cooper, 2003; Titus et al., 2007; Vauchez et al., 2012, and references therein), and seismic imaging and anisotropy (L. Zhu, 2000; Vauchez et al., 2012; Ford et al., 2014) further support the continuation of large strike-slip faults into the ductile portion of the lithosphere. However, each of the study methods has shortcomings (Vauchez et al., 2012), preventing an unequivocal conclusion. Studies on the same fault zone can yield conflicting results. For instance, Titus et al. (2007) find that observed seismic shear wave splitting in central California is consistent with a broad shear zone in the upper mantle beneath the San Andreas transform, while seismic imaging done by Ford et al. (2014) supports a zone of localized shear (less than 50 km).

Another example of a major transform is the Alpine fault in the South Island of New Zealand. Despite evidence from exhumed xenoliths and massifs for localized shear underneath the Alpine fault (e.g. Norris & Cooper, 2003; Kidder et al., 2021), geophysical evidence is less conclusive. Moore et al. (2002) use seismic shear wave splitting to conclude that the wide shear deformation on the surface mirrors that at depth. Lamb and Smith (2013) find that the surface velocity in South Island is fully explained by the deep slip on the main Australian and Pacific plate interface; the data does not require deep creep beneath individual faults in the region. For both the San Andreas fault zone in Southern California and the Marlborough fault zone in the South Island of New Zealand, an extension of the Alpine fault, Bourne et al. (1998) suggest that the surface velocity can be accounted for by a distributed shear zone below, without faults extending into the ductile region of the lithosphere. Consequently, the questions of whether faults extend beneath the brittle crust and whether the shear zone is localized or distributed remain unresolved.

The vast majority of studies addressing these questions have focused on large-scale continental transforms, with few investigations on smaller faults situated away from the immediate vicinity of continental boundaries. In this paper, we evaluate geodetic deformation across the Walker Lane, in California and Nevada, USA, a region that is not a major continental transform. We apply a quantitative analysis to compare the two competing models, addressing data uncertainties to identify significant parameters. We find little support for the presence of dislocations in the viscoelastic layer of the lithosphere and present strong evidence in favor of distributed shear deformation beneath the elastic layer, with faults terminating within the brittle crust.

2 Tectonic Setting

The Walker Lane (WL) (Figure 1a) is an elongated zone of both shear and extensional deformation in eastern California and western Nevada, separating the Sierra Nevada mountain range to the west from the Basin and Range Province to the east. The WL accommodates a substantial part of the relative active motion between the Pacific and North American plates (Bennett et al., 2003; Hammond et al., 2011). It is a dynamic and geologically complex region, exhibiting diverse topography and a variety of fault-

ing styles in complex network. It has been speculated that the WL is an immature continental boundary and will possibly become the main transform boundary in the future (Faulds et al., 2005; Wesnousky, 2005a; Pierce et al., 2021). Its northern section is characterized by northwest-striking, roughly parallel right-lateral strike-slip fault systems and northeast-trending left-lateral strike-slip faults (Wesnousky, 2005a). The deformation is predominantly shear in the region (Svarc et al., 2002; Hammond & Thatcher, 2004; Kreemer et al., 2009; Wesnousky et al., 2012; Kreemer & Young, 2022), associated with the translation of the Sierra Nevada/Central Valley microplate to the northwest with respect to the Basin and Range (Dixon et al., 2000; Argus & Gordon, 2001). The central WL, spanning from Walker Lake basin to Lake Tahoe basin, is characterized by a conspicuous absence of strike-slip faults (Wesnousky et al., 2012), with the exception of small north and northwest-trending strike-slip systems on the eastern side of the WL (Wesnousky, 2005a; Surpless, 2008; Dong et al., 2014; S. J. Angster et al., 2019; Pierce et al., 2021). A significant part of the motion in the central WL is accommodated by rotating crustal blocks and basins bounded by normal faults (Wesnousky et al., 2012; Bormann et al., 2016; Pierce et al., 2021).

3 Data Analysis

Modern high-precision GPS data achieve remarkable position accuracy (Blewitt, 2015; Bock & Melgar, 2016), which we improve to sub-millimeter levels through applying rigorous station selection criteria and position time series filtering. We use position time series in a North American plate reference frame, obtained from Nevada Geodetic Laboratory (Blewitt et al., 2018) and derived using the Precise Point Positioning method (more details in Kreemer et al. (2020)), using the GipsyX software by the Jet Propulsion Laboratory (JPL), and using JPL's final GPS orbits and clocks (Bertiger et al., 2020). The majority of the data were collected through the MAGNET GPS network, which utilizes a semi-permanent methodology (Blewitt et al., 2009), supplemented by data from continuously operating stations, mostly from the EarthScope Network of the Americas, but also from the Washoe County GPS Network and Leica SmartNet Network (Figure 1a).

We consider all time-series in the period 2007.0-2023.0 that span at least 2.5 years. We apply a station motion model to the time-series that includes annual and semi-annual sinusoidal signals, accounts for offsets, and iteratively removes outliers defined by $> 3\sigma$ deviation in the residual time-series. Offsets are obtained from the list of potential discontinuites from GNSS equipment changes earthquakes available at the Nevada Geodetic Laboratory (http://geodesy.unr.edu/NGLStationPages/steps.txt). Accidentally unrecorded or erroneously introduced offsets in position-time series can result in larger errors in velocities, especially for the semi-continuous stations. We meticulously screen each station for unrecorded equipment offsets and assess the impact of nearby earthquakes on the data. Earthquake-related offsets are introduced only when there is clear evidence that the station had been affected in a manner consistent with the earthquake's mechanism.

The time-series may sometimes be affected by non-tectonic processes, specifically hydrologic loading, which is more substantial for stations in the Sierra Nevada compared to those in the Great Basin. Not accounting for those signals can have an adverse effect on the station velocity, particularly for the semi-continuous stations. To best remove those signals, we apply a local common-mode filter to the data, using the method of Kreemer and Blewitt (2021), which effectively removes non-secular signals, leading to improved velocity estimates and smaller velocity uncertainties. In this method, only stations with >2000 position estimates are considered as filter stations (i.e., essentially the continuous stations and some of the frequently observed MAGNET stations) unless their residual time-series are not representative of the regional common-mode (see Kreemer and Blewitt (2021) for details) (Figures 1b and 2). Finally, we use MIDAS, a robust median

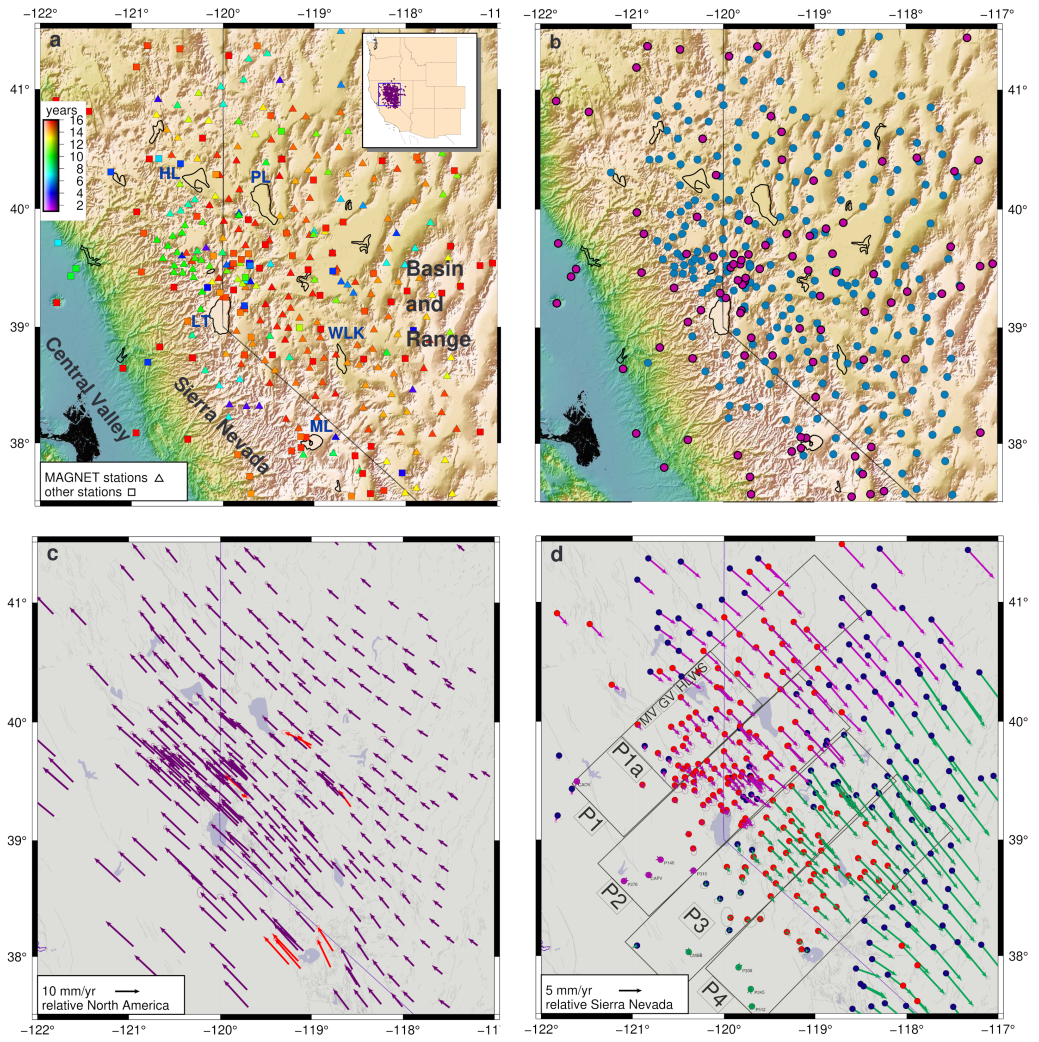

Figure 1. (A) Topographic map of the northern and central Walker Lane, showing major geologic features and lakes (Honey Lake – HL, Pyramid Lake – PL, Lake Tahoe – LT, Walker Lake – WLK), and the GPS stations (MAGNET stations are triangles), color-coded by the length of the time series. The inset shows the location of the map in the western United States and the stations used in the data processing and analysis (purple dots). (B) Stations used for filtering the GPS time series (purple dots) versus other stations (blue). (C) Shows the velocity field in a North America reference frame and the GPS stations omitted from the analysis (red vectors). (D) Map showing the two sets of reference stations (green and purple dots), the velocity field in the Sierra Nevada reference frame (color-coded with the reference stations), the strike-slip faults in the northern Walker Lane (MV – Mohawk Valley, GV – Grizzly Valley, HL – Honey Lake, and WS – Warm Springs), and the four profiles P1(a), P2, P3, and P4. For each profile, zero is defined as the western edge of the profile. The station dot color denotes the bounds of the shear zone based on the deviation of station velocity azimuth from the rotation field of the Sierra Nevada (red – less than 1.5° difference).

trend estimator (Blewitt et al., 2016), on the filtered and offset-corrected time-series to obtain each station's velocity and its uncertainty. The velocity field relative to North America is shown in Figure 1c for the 368 stations considered. Some stations with outlier velocity (typically observed for stations near active geothermal production areas) are identified and excluded from the remaining analysis. Data Set S1 contains the velocities used henceforth.

The velocities used in this analysis are not corrected for postseismic relaxation. Postseismic response of the viscoelastic lower crust and upper mantle following large earthquakes can last tens to hundreds of years and can affect geodetic velocities (Nur & Mavko, 1974; Savage & Prescott, 1978; Hammond et al., 2009). We explored the impact of correcting the velocities on our results in Supplemental Materials. While there are some differences, using the corrected velocity field yields the same conclusions that we are presenting here.

4 Modeling

4.1 Geodetic Profiles Across The Shear Zone

The Sierra Nevada (SN) west of the WL has been previously shown to have little internal deformation (Argus & Gordon, 1991; Dixon et al., 2000; Bennett et al., 2003; McCaffrey, 2005; Kreemer et al., 2009) and, therefore, provides a natural reference frame in which to analyze the velocity field across the WL. For this purpose, we use several long-term continuously-operating stations located on the rigid SN block to rotate the velocity field into a SN reference frame (Figure 1d). In doing so, we find that the residual motion of the SN sites is best reduced if we consider two distinct sets of reference stations, a northern and central set of five and four stations. By breaking up the SN into two different reference blocks, we also insure that our profiles across the WL optimally cover the area. We subsequently estimate two Euler poles, one for each group of stations, and use them to create two different reference frames. That is, we use those poles to rotate the original velocity field in the northern part of our study area into a northern SN fixed reference frame, and the central part into a central SN frame (Figure 1d). If the velocity field reflects shear in the WL, one would expect the SN fixed velocities to be parallel to small circles around the Euler poles. Because we expect stations in the east to start to reflect Basin and Range extension, we use the deviation of station velocity azimuths from the small circle azimuth within a specified tolerance as an estimate for the eastern boundary of the shear zone.

To examine the deformation, we define four profiles across the northern and central WL, labeled P1 in the north through P4 in the south (Figure 1d), oriented such that the along-profile components of velocity within the shear zone, defined by the velocity azimuths (Figure 1d, red dot stations), are minimized. We use the northern SN frame for P1 and P2 and the central SN frame for P3 and P4. The velocity profiles are then obtained by projecting the velocities onto the profile-normal orientation.

The signals across all four of the resulting profiles are similar in shape, with uniformly increasing across-profile velocities (Figure 2, blue dots) tapering off on the SN in the west and the Basin and Range in the east. There are no obvious inflections which might imply locations of the faults. The along-profile velocity component (Figure 2, black dots) is essentially zero in P1 and P2, but has a small signal in the eastern sections of P3 and P4, likely due to the narrowing of the shear zone in the southward direction.

4.2 Elastic Dislocation Model

According to the EDM for vertical strike-slip faults, the profile velocity, v, is a function of the distance along the profile, x, the location of fault i in the profile, f_i, the slip

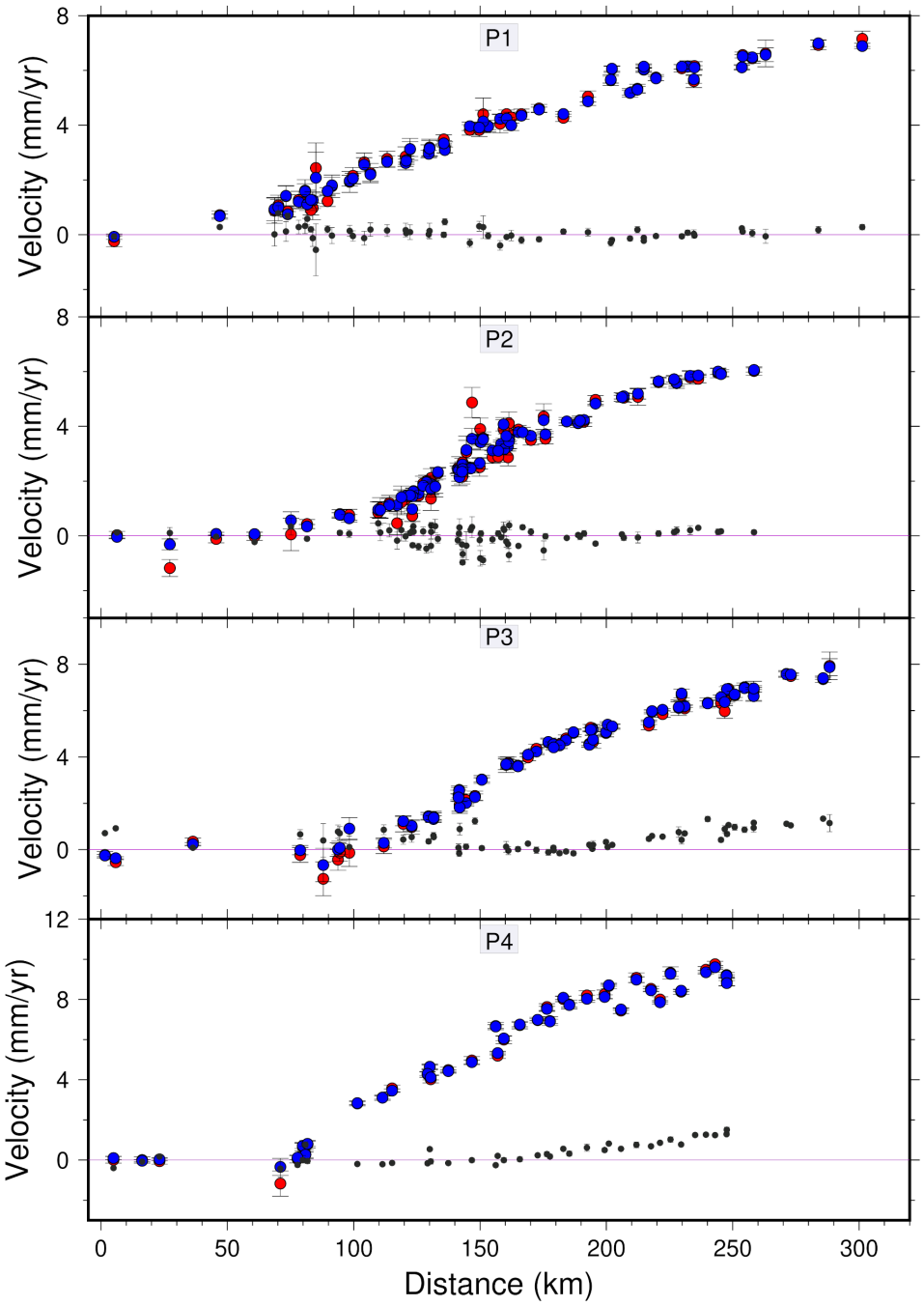

Figure 2. Velocity profiles P1, P2, P3, and P4 before (red) and after (blue) filtering. The outlines of the profiles are shown in Figure 1d. Note that the sign of the velocity is positive to the southeast in the SN frame. The velocity components that are along the direction of profiles are also shown relative to the northeast direction (black). The along-profile velocities are statistically not different from zero in P1 and P2 ($p>0.05$), but have a trend in P3 and P4 ($p<0.05$). This is due to the profiles being oriented to minimize the velocity vectors within the shear zone.

rate, s_i, and the locking depth, D_i, of each fault (Savage & Burford, 1973). Thus, we evaluate the EDM using the equation

$$v = \sum_{i=1}^{N} \frac{s_i}{\pi} arctan\left(\frac{x - f_i}{D_i}\right) \tag{1}$$

where N is the number of faults present in the profile.

Since the four strike-slip faults we are interested in are all on the western side of P1 (Figure 1d), we define a subset profile P1a, beginning and terminating to the west and east, respectively, of the set of the strike-slip faults (Figure 3). There are other, predominantly normal, faults in the eastern half of P1. Deformation due to dip-slip dislocations would have gradients in both strike-parallel and perpendicular velocity components. We do not observe a gradient in velocity when moving across the normal faults (Figure 2, black dots). Therefore, there is no need to consider any dislocation that would produce a strike-normal gradient, such as the north-south trending normal faults located in the eastern half of P1.

We combine the HL and WS faults into a single dislocation, HLWS, since the two are separated by only about 4-10 km. When the width of a deformation zone is less than the critical length, πD, the surface velocity due to any number of dislocations within the zone appears equivalent to that of a single dislocation, the one accommodating the majority of the total slip (Traoré et al., 2014). Consequently, it is impossible to differentiate between distributed shear and a single dislocation over such areas (Moore et al., 2002). In our case, the critical length is ∼50km. Profile P1a extends over a length of 115 km, theoretically allowing us to resolve at least two faults. We consider the MV fault on the western side of the profile and the combined HLWS faults on the eastern side as the two dislocations. This is similar to, e.g., the geodetic block model of Hammond et al. (2011).

We constrain each fault's locking depth, D_i, using the seismogenic depths (Ruhl et al., 2020; Zuza & Cao, 2020): 17km for MV and 14 km for HLWS faults. We consider the surface trace of the faults along with relocated seismicity clusters (Figure 3) in constraining the fault locations, f_i. We position MV fault above the obvious seismicity cluster and HLWS – approximately between the surface traces of the HL and WS faults. After constraining Di and f_i, Equation 2 for the EDM is linear in the remaining parameters, the slip rates s_i. Thus, we use a weighted linear least-squares approach to approximate the slip rates for the two dislocations.

4.3 Shear Zone Model

We adapt the parameterization of the SZM as described by Prescott and Nur (1981) and Prescott et al. (1981) (Figure 4). The strain field present on the surface above the shear zone is approximated by a distribution of infinitesimal screw dislocations. By integrating the strain field over the width of the shear zone, the surface velocity is obtained as a function of the distance across the fault x, the velocity difference across the shear zone b (i.e., total slip rate), the thickness of the elastic layer D, and the half-width w of the shear zone below depth D (Prescott et al., 1981):

$$\begin{aligned} v \;=\; & -\frac{b}{2\pi w}\Big[(x' - w)arctan\left(\frac{x' - w}{D}\right) - (x' + w)arctan\left(\frac{x' + w}{D}\right) \\ & -\frac{D}{2} ln\left(\frac{D^2 + (x' - w)^2}{D^2 + (x' + w)^2}\right)\Big] + bc \end{aligned} \tag{2}$$

where $x' = x - aw$. To determine the best-fit values for the parameters, we fit Equation 2 to the four profiles—P1, P2, P3, and P4—employing a weighted nonlinear least-

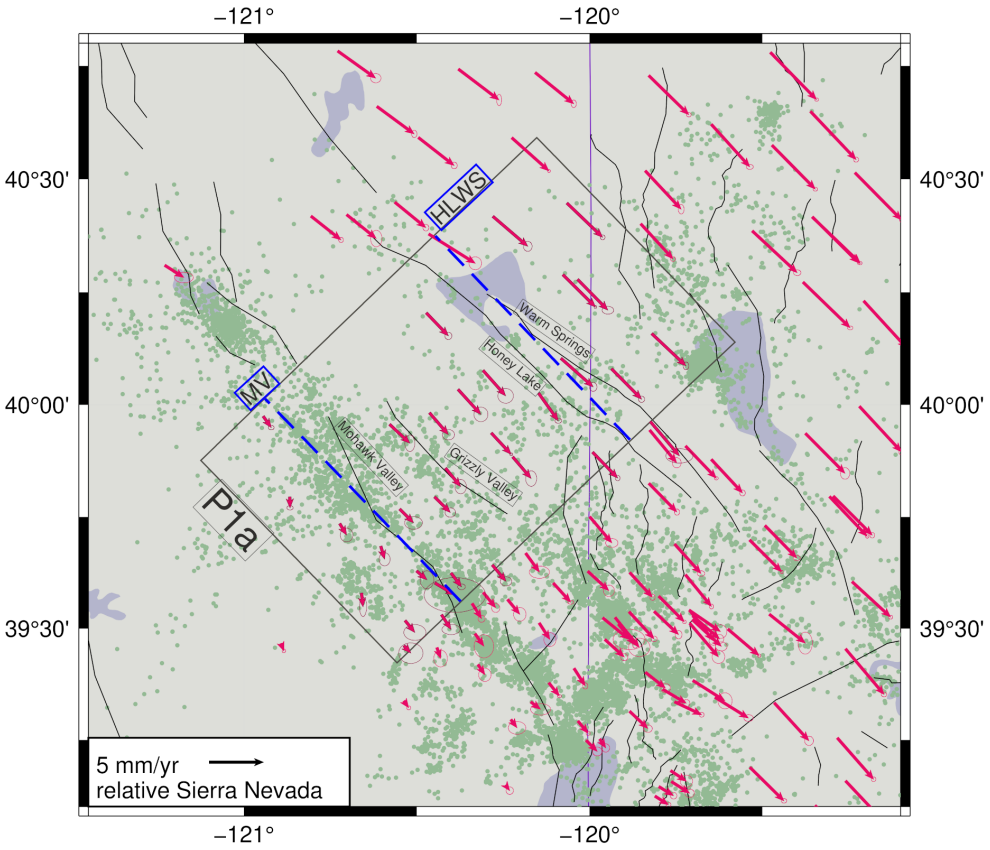

Figure 3. Map of the Northern Walker Lane, enlarged on profile P1a (gray box). Assumed Mohawk Valley (MV) and Honey Lake-Warm Spring (HLWS) fault locations are shown in blue dashed lines. The actual traces of the four strike-slip faults in the profile are also marked. Relocated seismicity (Ruhl et al., 2020) with m≥-1 between 2002-2019 is shown in light green.

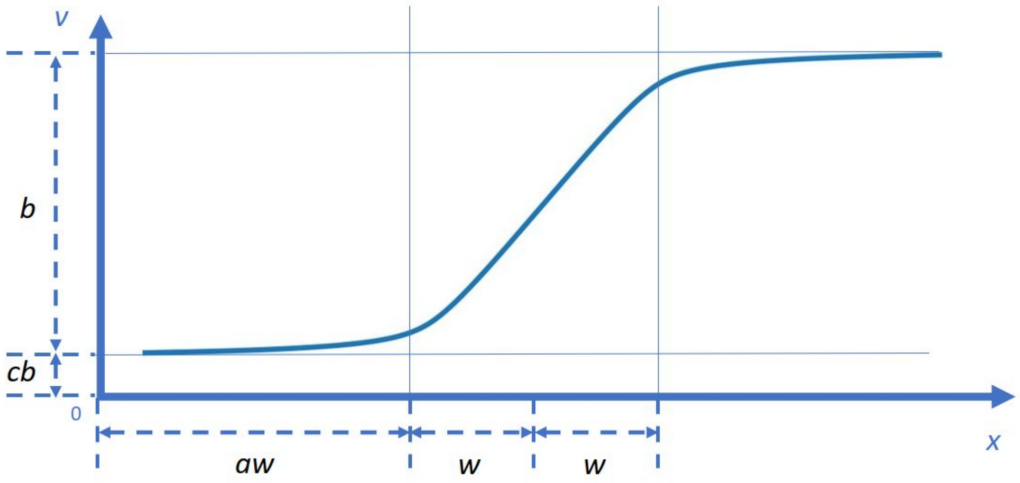

Figure 4. A diagram illustrating how Equation 2 characterizes surface deformation. The shear zone's half-width (w) is located at depth D, and b is the total velocity difference across the shear zone. Dimensionless factors a and c align Equation 2 with the location of the western edge of the shear zone within the profile (a shifts the function horizontally and c shifts it vertically).

squares approach. We tested values of for w and D in a grid search and plot RMS misfit values for each profile in Figure 5.

A trade-off exists between the parameters D and w due to the coupling between the elastic and the viscoelastic layers. A combination of a large value of D and a small value of w can result in surface velocities similar to those due to a small value of D and a large value of w. To constrain this problem, either D or w must be determined through alternative sources of data. The RMS contour plots reveal that the half-width parameter is well constrained by the data, while the depth is not. Relocated seismicity in the northern WL (Ruhl et al., 2020) indicates that the majority of seismic activity in the region takes place above 20 km. We therefore fix the upper bound for the value of D in Equation 2 to be 20 km, which is also near the minimum in RMS misfit at each profile (Figure 5). We use the shear zone width predicted by the velocity azimuths (Figure 1d) to compare with that predicted by the SZM, thus employing two independent methods for determining the shear zone bounds.

5 Results

The EDM fit to Profile P1a (Figure 6b) yields slip rates of 2.7 ± 0.1 mm/yr and 2.2 ± 0.1 mm/yr for MV and HLWS faults respectively. The sum of the predicted slip rates is 4.9 mm/yr, which is a 68% of the 7.2 mm/yr relative velocity budget observed across the entire shear zone in P1. This discrepancy does not necessarily favor one model over the other, since profile P1a is a subset of P1 and has its own relative budget of about 5 mm/yr across it. We do not fit the EDM to the entire shear zone for reasons described in section 4.2. The linear model-predicted strain rate across the zone (slope of the line) is 37 nanostrains/yr, which is in agreement with the shear strain calculated by Kreemer and Young (2022). We obtain excellent SZM fits for each of the four profiles (Figure 7) and find good agreement between the model-predicted shear zone width, w, and that predicted by the velocity azimuths. The width of the shear zone is estimated to be the widest, 172 ± 6 km, in the northern end of the WL. It then narrows to 130 ± 4 km near Lake

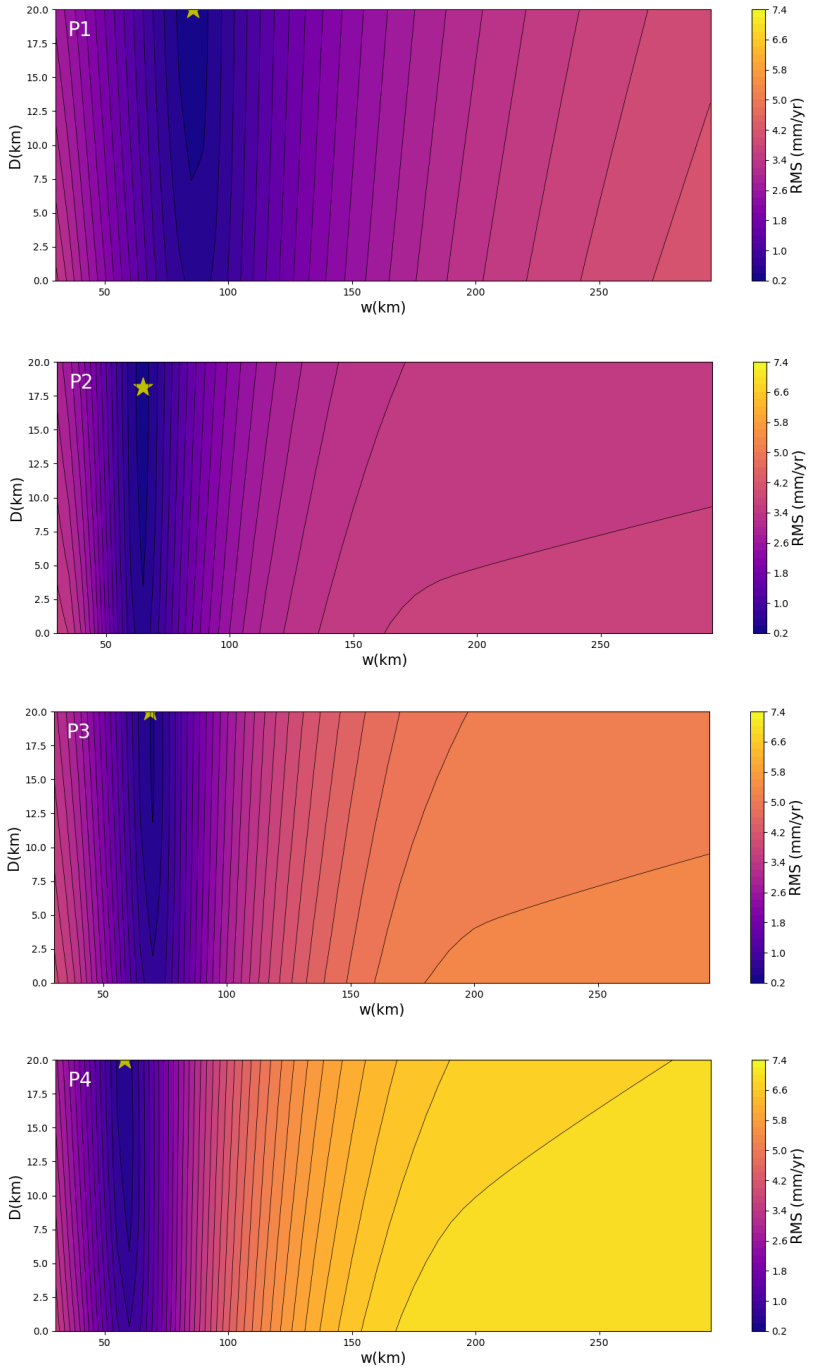

Figure 5. RMS of residual velocity data contour plots for the thickness of the elastic layer (D) and the half-width of the shear zone (w) in the Shear Zone Model (Equation 2) for profiles P1, P2, P3, and P4. The gold stars denote the best-fit results when we solve for both parameters, but having set an a priori maximum depth to 20km).

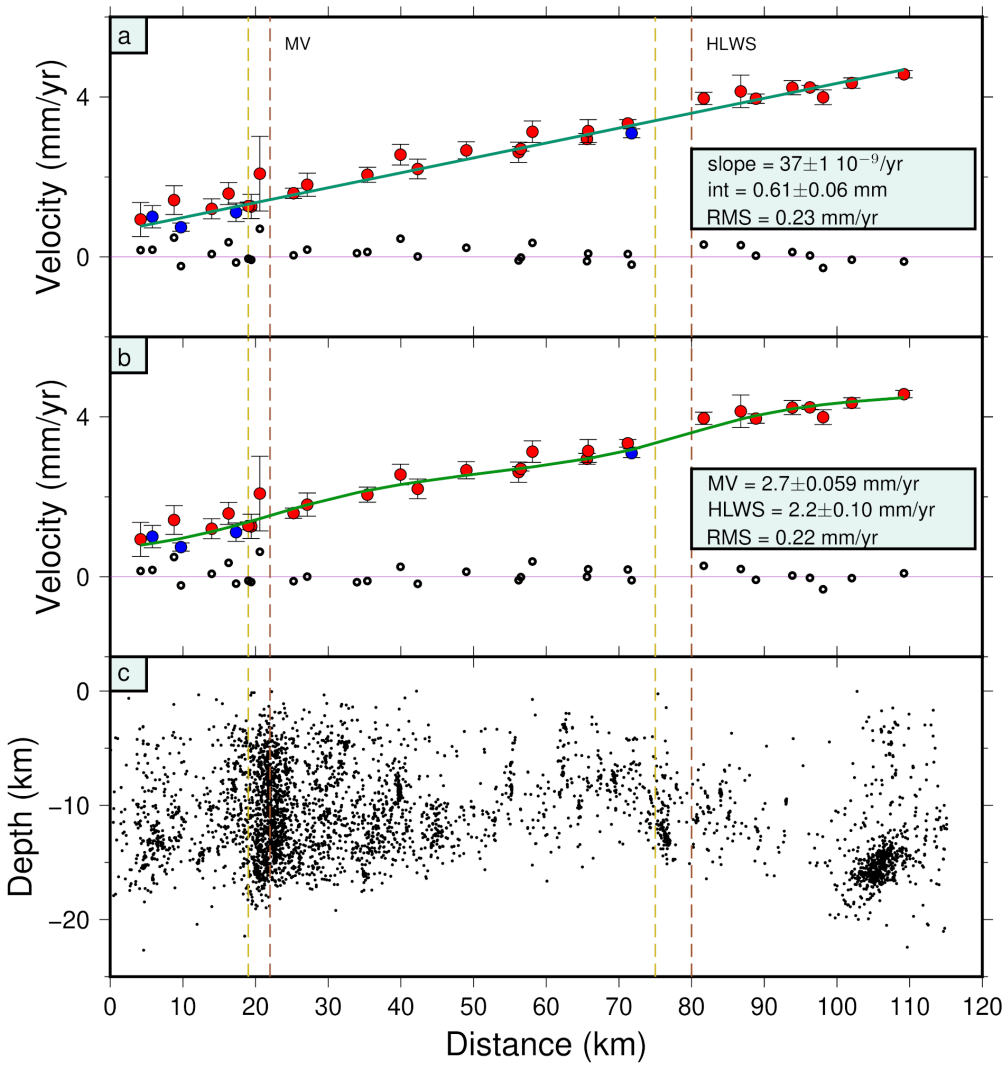

Figure 6. Profile P1a fault-parallel velocities are shown with the linear model (a) and the elastic dislocation model (b) fits. The locations of the faults are indicated by the dashed lines: brown – constrained using the surface fault traces, yellow – obtained by minimizing the misfit to the Elastic Dislocation Model (EDM) fit (Equation 1). The locking depths are constrained to be equivalent to seismogenic depth. The predicted parameters for the line and the EDM (slip rates of each fault) are listed. Relocated seismicity (Ruhl et al., 2020) with m≥-1 between 2002-2019 is shown in the bottom panel (c).

Tahoe and 138 ± 6 km south of Lake Tahoe, before further narrowing to 116 ± 4 km (Figure 7, vertical dashed lines). Profiles P1, P3, and P4 are best-fit with a depth of 20 km, the upper bound placed on D. P2 prefers a depth of 18 km. The best-fit depths of all profiles are within uncertainty of each other. The total relative velocity across the shear zone is 7.2±0.3 mm/yr, 6.8±0.2 mm/yr, 8.4±0.2 mm/yr, and 10.1±0.2 mm/yr for P1, P2, P3, and P4 respectively.

6 Discussion

The favorable fit of the SZM to the geodetic profiles suggests that the deformation of the lower crust in the WL region is characterized by distributed viscous shear. However, the observed geodetic strain can also be explained by the combined effect of EDM-related deformation across multiple faults, if the slip is roughly equally distributed among the dislocations. The presence of the near-vertical strike-slip faults in the northern section of the WL allows us to explore this possibility.

We show that both models fit the data quite well, as indicated by the data misfit. We cannot say whether one model fits better than the other, since direct statistic comparison of EDM and SZM is not possible since profile P1a is a subset of profile P1. However, due to the linear nature of the SZM, we can make a direct comparison between the EDM fit and a linear model fit to the same profile P1a.

6.1 Elastic Dislocation Model

The linear fit to profile P1a (Figure 6a) yields an RMS value of 0.23 mm/yr, which is essentially same as the RMS of the EDM (0.22 mm/yr). If the deformation is accommodated by elastic dislocations, there are several possible reasons for the lack of a clear preference for the EDM over the linear model: (1) the noise in the data obscures the EDM, (2) the modeled fault locations or locking depths do not correspond to reality, (3) there are unknown dislocations present, and (4) the faults are late in their seismic cycles.

6.1.1 Is EDM Hiding in the Noise?

To address hypothesis (1), we estimate the likelihood of the observed result, assuming the presence of an EDM in the data. To that end, we construct synthetic data using Equation 1 with fault parameters identical to those in profile P1a. We then generate 100K realizations of noisy synthetic data by adding noise to the predictions of the model. The noise is randomly chosen from a normal distribution with a mean of zero and a standard deviation of 0.22 mm/yr, the estimated level of uncertainty in our GPS velocity data. We fit the line and the EDM to each of the noisy synthetic datasets and count how often the RMS of the EDM is smaller than that of the line by more than 0.01 mm/yr. Our findings indicate that there is a 78% likelihood of us being able to recover the EDM from the synthetic noisy data. This suggests that it is unlikely that the signal of EDM faults is obscured by the noise in the real data.

6.1.2 Are There Better Fault Locations or Locking Depths?

Regarding hypothesis (2), we note that the WL is an immature fault zone characterized by a complex geometry. For the purposes of modeling, the faults are represented as single straight lines, so there is a margin of error to the locations of the faults in the profile. The locking depths of each fault are similarly uncertain. To address the location uncertainty, we search for alternative fault locations within the profile that would result in a better fit of the EDM to the data. We test possible fault configurations by allowing each fault to vary its location between the nearest profile edge and the midpoint of the profile. We then fit each configuration with the EDM and search for a reduction in

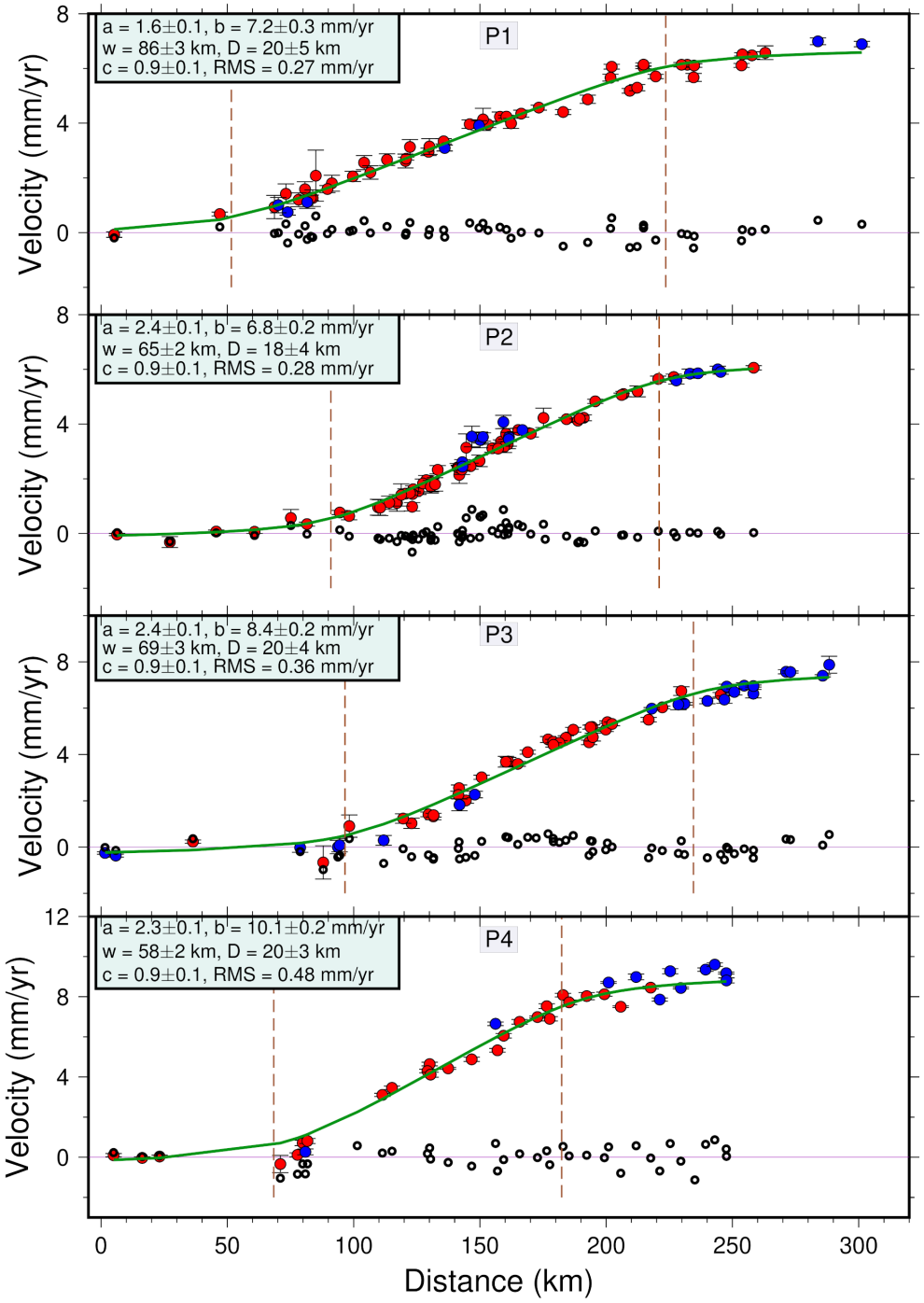

Figure 7. Shear Zone Model fits (Equation 2) to the across-profile velocity components are shown (the sign of the velocities is flipped). Station dots are color coded as in Figure 1d based on velocity azimuth. Best-fit model parameters are listed for each profile: horizontal shift factor a, velocity difference across the zone b, half-width of zone w, thickness of the elastic layer D, and the vertical shift factor, c. Model-derived shear zone widths at depth D are shown in dashed vertical lines. Residuals to the fit are also shown (small black circles).

the RMS error. We employ a similar approach to assess the uncertainty in the locking depths of the faults, allowing the depths to vary between 2 and 30 km.

Our findings reveal that the fault locations that minimize the misfit are approximately 19 kilometers for MV and 75 kilometers for HLWS. These locations are very close to the assumed (3 km difference for MV and 5 km for HLWS), but do not appear to correlate to seismicity clusters and result in an insignificant reduction of RMS by only 0.01 mm/yr. The preferred locking depths, which result in the same reduction in RMS as the optimal locations, are approximately 15 kilometers for MV and 30 km for HLWS faults. While 15 km locking depth for MV is feasible, the locking depth for the HLWS is unrealistic, considering that relocated seismicity predicts a much shallower seismogenic thickness of about 14 km.

An RMS contour plot for the locking depths of the two faults (Figure 8) indicates that the locking depths are poorly constrained by the data, suggesting that using seismogenic depths as a priori constraints may be more suitable for the analysis. The contour plot for the locations of the faults shows that the location of MV is well constrained, however there is much less preference for the location of the HLWS fault. The latter is surprising, since the surface velocity in the EDM is driven by the location of the faults. This is another feature of the data that is inconsistent with the downdip extension of the HLWS.

6.1.3 Are There Unknown Dislocations?

Testing hypothesis (3), i.e., that there are additional dislocations present, presents a challenge due to the limitations imposed by the relatively short length of the profile. Given that the seismogenic thickness in the region varies between approximately 10 to 20 km, the critical length, πD, is between 30 and 63 km. The length of profile P1a is 115 km, which is 1.9 to 3.8 times the critical length, meaning that we may be able to resolve a third dislocation, but no more.

We find that, despite a preference, the model's fit is not highly sensitive to the location of the third dislocation: the difference between the minimum and maximum RMS values is less than 0.02 mm/yr. If we begin the search with the initially assumed locations of MV and HLWS, the predicted location for the third fault falls between the western edge and 21 km or between 57 km and the eastern edge of the profile, with an RMS value of 0.22 mm/yr (Figure 9, brown line). If we initiate the search with the best-fit locations of MV and HLWS, as described in the previous paragraph, the predicted location range of the third fault is similar, with an RMS of 0.21 mm/yr (Figure 9, orange line). Any location within these ranges provides an equally good fit, but the reduction in the RMS is essentially zero (ΔRMS < 0.001 mm/yr). There is evidence for the existence of a strike-slip zone (Pyramid Lake fault zone, Eisses et al., 2015) in the easternmost section of this location window. However, the result of our analysis suggests either that we are unable to resolve dislocations beyond the two already considered, or that additional dislocations are not necessary, as they do not significantly enhance the fit of the EDM.

6.1.4 Are the Faults Late in their Seismic Cycle?

Concerning hypothesis (4), several authors (e.g. Wang et al., 2021) point out that the effects of coupling between the brittle upper crust and underlying viscoelastic layers on the earthquake cycle (Savage, 2000) cannot be ignored. The rate of strain accumulation slows with time since last earthquake t, making the surface velocity appear more linear late in the seismic cycle, i.e., if the time since the last event is significantly longer than the relaxation time τ. Geological studies of past seismic events show that the MV (Gold et al., 2014) is about mid-cycle, HL (Wills & Borchardt, 1993) is mid-cycle or less

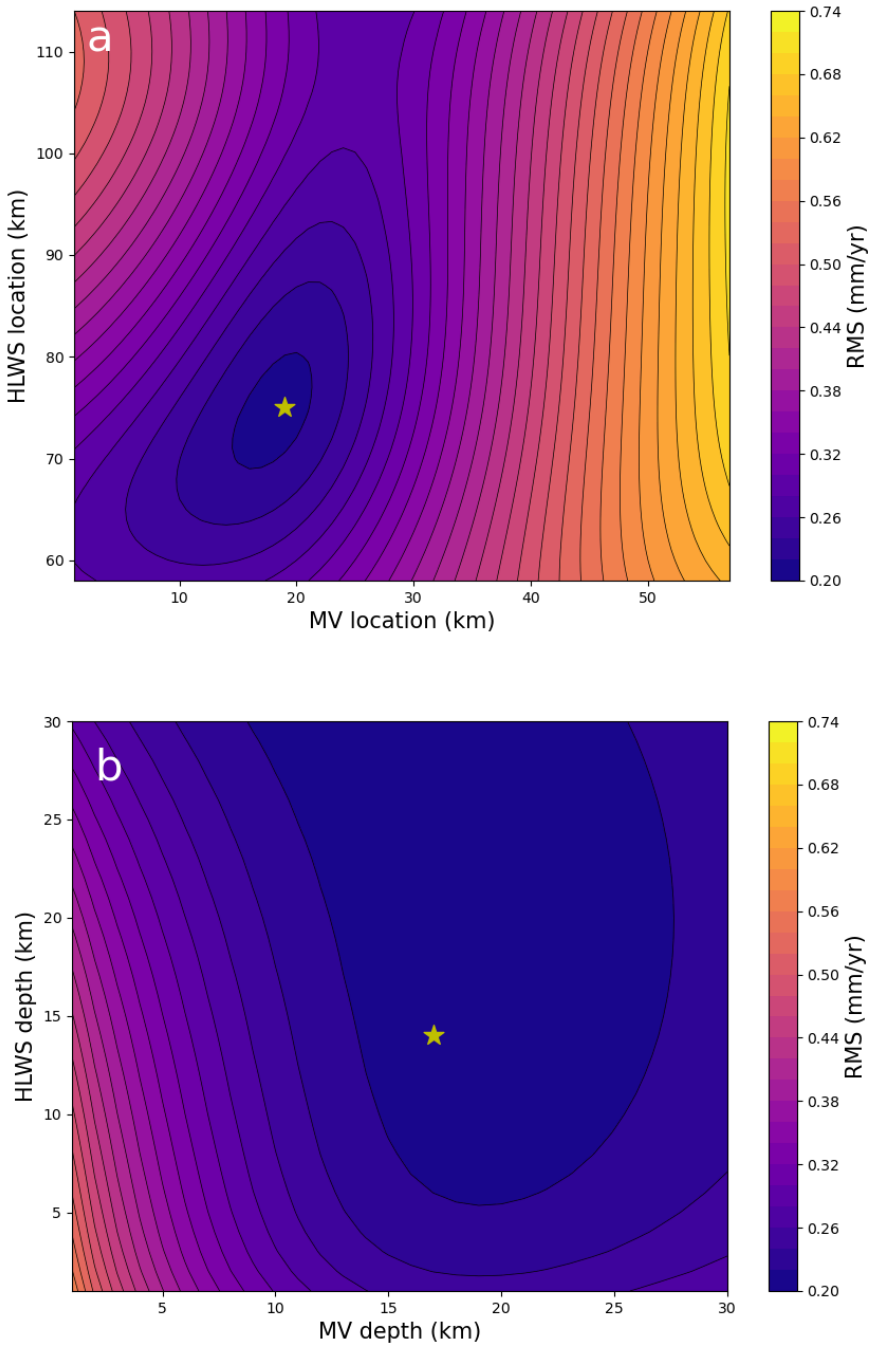

Figure 8. RMS contour plots for the locations (top) and locking depths (bottom) of the two modeled faults in profile P1a (i.e., HLWS = Honey Lake and Warm Springs faults, and MV = Mohawk Valley). The gold stars denote the best-fit locations and assumed depths for the purposes of fitting the EDM.

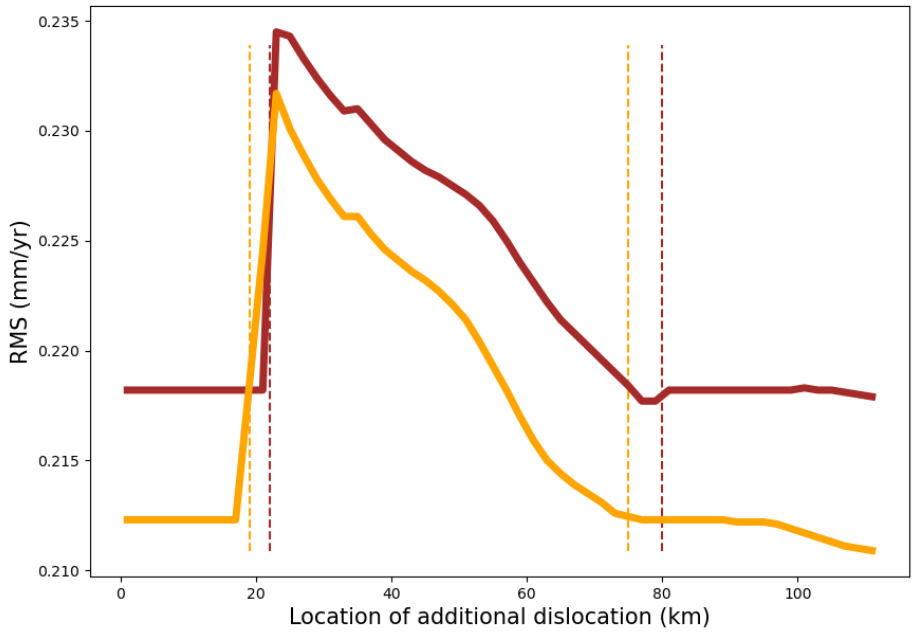

Figure 9. RMS misfit from a three-fault Elastic Dislocation Model as a function of the location of the third fault. Brown line is starting with assumed a priori locations of MV and HLWS faults, orange – best-fit locations (section 6.1.2). The locations of the MV and HLWS faults are shown in orange (best-fit) and brown (assumed a priori) dashed lines. Note that the difference between minimum and maximum RMS is less than 0.02 mm/yr.

(latest seismic event within a few hundreds of years), and WS (Chupik et al., 2022) is as early as ∼100 years into its cycle. Taking a typically-reported viscosity for the lower crust, 10^{20} Pa s (e.g. Bills et al., 2007; Hammond et al., 2009), the ratio of the earthquake recurrence time T to τ is longer than 15 for any of the faults in the northern WL. These values may be large enough to cause the velocities across the faults look linear, however the faults are in different stages of their seismic cycles, so it is reasonable to expect differences in the slope of the velocity profile across them, which we do not observe. Furthermore, we have profiles P2, P3, and P4, which provide more opportunities for the faults within them to exhibit that they are in different times of their relaxation cycles. However, all profiles show similar linearity, increasing the likelihood that we are not detecting time since last seismic event with GPS velocities.

6.2 Shear Zone Model

We examined potential reasons for the lack of a clear preference for the EDM in profile P1 and found no compelling explanations. Despite different faulting styles captured by P2, P3, and P4, their velocity profiles have similar characteristics as in P1. We will now present arguments supporting the presence of a distributed shear zone in the lower crust.

6.2.1 Support for Distributed Shear Zone

Distributed seismicity in the region (Figure 10) supports the idea of distributed deformation of the lower crust. Specifically, with the exception of the MV fault, seismicity within profile P1a does not seem to correlate strongly with known faults. The diffuse seismicity implies that the lower crust within the WL is deforming more evenly than would be predicted by focused deep dislocations which transfer stress upward into the upper crust.

Lack of dislocation continuation into the ductile portion of the crust is also supported by seismic imaging of the Warm Springs fault zone (Briggs et al., 2021), which revealed that the fault sections truncate at a depth of 8-12 km, intersected by a mid-crustal low-angle fault. Furthermore, uniformly featureless character of the velocity profiles is a strong argument for distributed shear. Despite significant geological variations and differing faulting styles from north to south and from west to east, all four velocity profiles exhibit the same shape. This similarity suggests that the same mechanism is responsible for surface deformation in all of these profiles.

The presence of a distributed shear zone in the lower crust aligns with the observations of the surface features in the central WL. The presence of en echelon basins and rotated crustal blocks has been shown to be consistent with a uniformly shearing viscoelastic layer, capped by the brittle upper crust (Wesnousky et al., 2012). The rotating crustal blocks can be interpreted as rigid blocks riding on the underlying viscoelastic layer (Prescott & Nur, 1981; Wesnousky, 2005a).

6.2.2 Summary of Arguments for Distributed Lower Crustal Shear

Several factors support the SZM as the correct model:

1. The velocity profiles appear linear and the data is well-explained by the SZM (Figure 6).
2. The SZM-predicted shear zone width aligns with that derived from the velocity azimuths (Figures 6 and 10).
3. The SZM-predicted bounds of the shear zone coincide with the edges of seismicity in the region (Figure 10).

4. The velocity profiles appear to be independent of fault geometry: it is impossible to determine fault locations within each profile without prior knowledge of their locations.
5. Despite diverse surface features, all four profiles exhibit spatially consistent velocity profile shapes, suggesting a common deformation mechanism.
6. The faults are in different stages of their seismic cycles, yet that is not reflected in the uniformly linear velocity profiles.
7. Distributed seismicity in the region supports the idea of distributed deformation of the lower crust.

6.3 Implications

6.3.1 Tectonics

The observed distributed shear supports the conclusions of other studies that suggest the WL is a structurally immature plate boundary (Faulds et al., 2005; Wesnousky, 2005b). Norris and Toy (2014) suggest a model for transform fault evolution, in which major continental boundary transforms begin as zones of broadly distributed shear, characterized by a number of smaller faults. These faults are limited to the seismogenic crust, eventually propagating into the lower crust and upper mantle due to positive feedback loops as the transform boundary matures. In this view, the dislocations in the WL will eventually organize into straighter and longer transform faults, which may develop localized shear in the ductile lower crust and upper mantle.

Distance along the WL can be considered a proxy for the geological time, with the northern section being the youngest. Our findings show southward narrowing of the shear zone, indicating that the WL is becoming narrower over time. This supports the idea of the WL transforming into an incipient transform boundary.

We identified a distributed shear zone as the cause of surface deformation in the WL. However, we cannot distinguish whether the system is being driven from the sides (i.e. the Sierra Nevada block motion relative to the Basin and Range) or from below (Savage, 2000). Barbot (2020) shows that the lower crust/upper mantle flow in the northern and central WL is uniform, and presents evidence that the brittle crust is mechanically coupled to the ductile portion of the lithosphere. This implies that the surface deformation in the WL, as well as the rotation of the Sierra Nevada, are ultimately driven by the deep interaction between the Pacific and North American plates.

6.3.2 Consistency with Other Observations Suggesting Lower Crustal Flow

The absence of dislocations in the lower crust is consistent with ductile flow since substantial flow would inhibit the progressive development of stable planar zones of shear. Moreover, the time scale of flow observed in the lower crust tends to be shorter than earthquake recurrence times, suggesting weakness of the lower crust on geologic time scales. The time scales of flow are indicated by studies of postseismic relaxation and isostatic rebound (Bills et al., 2007; Freed et al., 2007; Hammond et al., 2009; Dickinson et al., 2016), which estimate viscosities of about 10^{20} Pa s. This value implies that the relaxation time for the lower crust is on the order of hundreds of years, which is short compared to the earthquake recurrence intervals of thousands of years. This is also supported by seismic reflection observations of Moho topography which is different from the surface topography (Hauge et al., 1987; McKenzie et al., 2000), as well as a very thin apparent elastic plate thickness in the Basin and Range estimated from the lack of coherence between gravity and topography (Lowry & Smith, 1994).

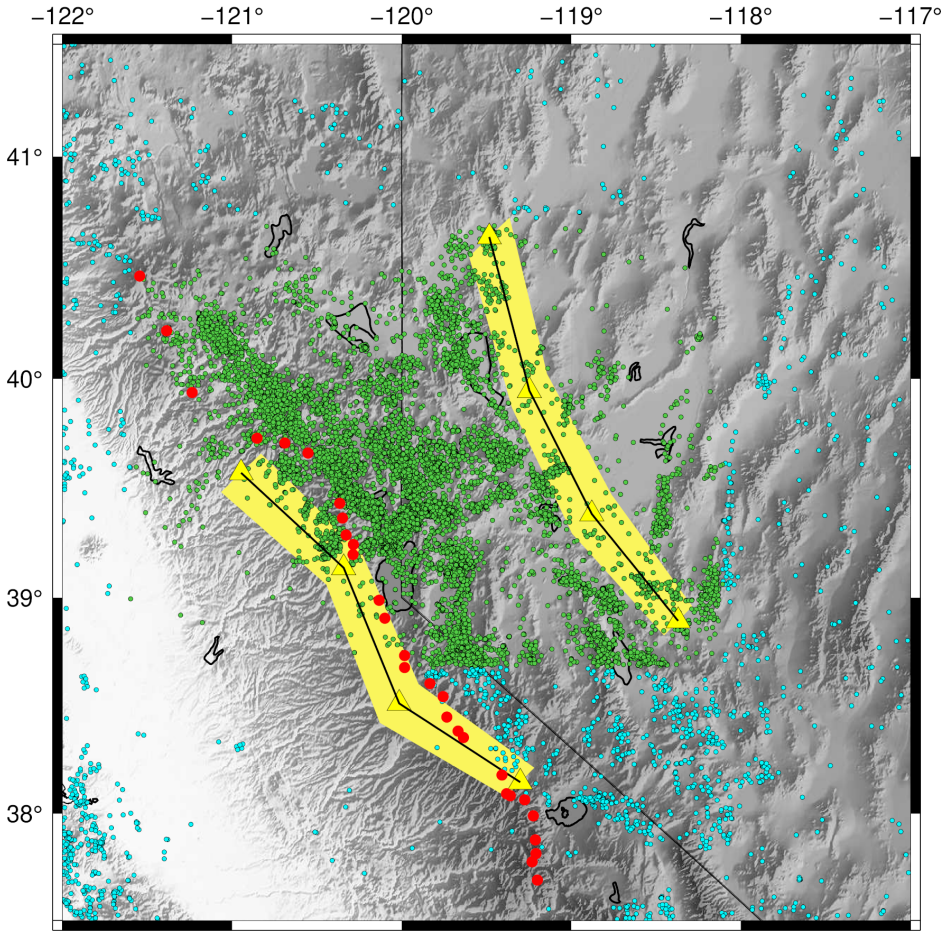

Figure 10. The map from Figure 1 is shown with the shear zone outline (black lines), predicted by the Shear Zone Model. Yellow shaded areas represent the uncertainty of the shear zone boundaries. Yellow triangles denote the location of the edges of the shear zone below the elastic layer of the crust in each profile. Relocated seismicity (Ruhl et al., 2020) with m≥-1 between 2002-2019 is plotted in green where available, ANSS/ComCat mainshocks with m≥2 between 2003-2020 are plotted in blue elsewhere. Red dots are the tallest regional peaks, plotted as a proxy for the Sierra Nevada crest.

6.3.3 Fault Slip Rates

Our findings raise questions about the possibility of estimating slip rates on individual faults using geodetic data in areas where the surface velocities reflect distributed shear deformation. Bourne et al. (1998) suggested that the slip rates of individual faults are controlled by their number and location within the shear zone, not by deep dislocations beneath the faults. In this view, the slip rates are obtained by distributing the far field velocity budget onto the faults within the velocity profile. The slip rate on a given strike-slip fault is the difference between average velocities on either side of the fault. However, in the WL, this method can only be applied to the MV and, perhaps, the GV faults, since the shear zone extends horizontally past the strike-slip faults into an area characterized by normal faulting. Following the Bourne et al. (1998) approach, the slip rate for the MV fault is 0.72 mm/yr, which is within the range of permissible geologic rates with a minimum 0.4 mm/yr (Sawyer et al., 2013). Including the GV fault yields slip rates of 0.28 mm/yr for MV and 0.52 mm/yr for GV. The only geologic slip rate available for the GV fault is the general estimate of <1 mm/yr (Gold et al., 2013), with which our estimate agrees. However, that would imply that the slip rate for the MV fault is smaller than the minimum inferred geologic estimate.

The SZM predicts that the total upper crustal fault slip rates across the entire shear zone should agree with geodetic estimates of far field motion, about 7 mm/yr to 10 mm/yr (depending on profile P1-P4). The sum of maximum geologic slip rates (rate plus uncertainty) on documented faults captured by profile P1a (Gold et al., 2013; Sawyer et al., 2013; Gold et al., 2014, 2017; S. Angster et al., 2016) aligns with the geodetic velocity budget across profile P1a of approximately 5 mm/yr. This leaves at least 2 mm/yr to be accommodated by the normal faults in eastern part of P1, however it is unclear how they accommodate the shear.

A discrepancy between the total geodetic slip and that obtained by summing the geologic slip rates on the known faults has been noted (Hammond et al., 2011; Gold et al., 2014; Bormann et al., 2016; S. J. Angster et al., 2019). In the central WL, the missing geological slip has been attributed to the block rotations and strike-slip faults that may be missing from the geologic datasets (Dong et al., 2014; Bormann et al., 2016; Pierce et al., 2021). It is probable that processes like those occurring in the central WL may also be in effect in the northern WL. However, the vertical axis block rotations in the central WL are partly accommodated by east-northeast striking sinistral faults (Wesnousky, 2005a; Wesnousky et al., 2012; DeLano et al., 2019), which are not present in the northernmost WL. The lack of vertical axis rotations in the northern WL simplifies the estimation of the SZM-geodetic slip rates and makes comparison with geologic rates more straightforward. In any case, using the SZM-based geodetic slip rates does not in and of itself explain the discrepancy between geologic and geodetic slip rates, nor does it make the discrepancy worse. It does, however, change some of the details in the geodetic slip rates estimates and could lead to somewhat different estimates of seismic hazard distribution, if it is based on SZM-based geodetic slip rates.

7 Conclusion

Our study challenges the use of elastic dislocations with deep creep for explaining active deformation along faults everywhere. Geodetic evidence in the northern and central Walker Lane supports a distributed shear zone in the lower crust. This suggests that faults likely terminate near the bottom of the upper crust. Consequently, models based on discrete dislocations in the viscoelastic lower crust are not appropriate to estimate the slip rates on the individual faults. A more suitable approach in these locations is to consider how the total relative velocity budget is distributed among the faults, potentially based on the location and azimuth of the fault within the shear zone.

8 Open Research

All data used in this research can be accessed freely on the Nevada Geodetic Laboratory website (http://geodesy.unr.edu). The GPS data has been collected through the MAGNET GPS network, EarthScope Network of the Americas (Community, 2006), the Washoe County GPS Network, and Leica SmartNet Network. Maps and figures were created with Matplotlib version 3.7 (Hunter, 2007) (https://matplotlib.org/) and Generic Mapping Tools (GMT) version 6 (Wessel et al., 2019) (https://www.genericmapping-tools.org/).

Acknowledgments

This work has been partly supported by funding from the Office of Energy Efficiency and Renewable Energy (EERE), U.S. Department of Energy, under Award Number DE-EE0009032, and NSF award 1914501. Surveying of the MAGNET GPS network and analysis was supported by the USGS Geodetic Networks program cooperative agreements G10AC00138, G15AC00078 and G20AC00046, and USGS research grants 08HQGR0027 and G11AP20023. GPS data processing is supported by NASA grant number 80NSSC22K0463. This material is based on services provided by the GAGE Facility, operated by UNAVCO, Inc., with support from the National Science Foundation, the National Aeronautics and Space Administration, and the U.S. Geological Survey under NSF Cooperative Agreement EAR-1724794. Part of the data for this project was collected by Washoe County GPS Network and Leica SmartNet Network.

References

Angster, S., Wesnousky, S., Huang, W., Kent, G., Nakata, T., & Goto, H. (2016). Application of UAV Photography to Refining the Slip Rate on the Pyramid Lake Fault Zone, Nevada. *Bulletin of the Seismological Society of America*, *106*(2), 785–798. doi: 10.1785/0120150144

Angster, S. J., Wesnousky, S. G., Figueiredo, P. M., Owen, L. A., & Hammer, S. J. (2019). Late Quaternary slip rates for faults of the central Walker Lane (Nevada, USA): Spatiotemporal strain release in a strike-slip fault system. *Geosphere*, *15*(5), 1460–1478. doi: 10.1130/GES02088.1

Argus, D. F., & Gordon, R. G. (1991). Current Sierra Nevada-North America motion from very long baseline interferometry:Implications for the kinematics of the western United States. *Geology*, *19*(11), 1085–1088. doi: 10.1130/0091-7613(1991)019⟨1085:CSNNAM⟩2.3.CO;2

Argus, D. F., & Gordon, R. G. (2001). Present tectonic motion across the Coast Ranges and San Andreas fault system in central California. *GSA Bulletin*, *113*(12), 1580–1592. doi: 10.1130/0016-7606(2001)113⟨1580:PTMATC⟩2.0.CO;2

Barbot, S. (2020). Mantle flow distribution beneath the california margin. *Nature Communications*, *11*(1), 4456. doi: 10.1038/s41467-020-18260-8

Bennett, R. A., Wernicke, B. P., Niemi, N. A., Friedrich, A. M., & Davis, J. L. (2003). Contemporary strain rates in the northern Basin and Range province from GPS data. *Tectonics*, *22*(2), 2001TC001355. doi: 10.1029/2001TC001355

Bertiger, W., Bar-Sever, Y., Dorsey, A., Haines, B., Harvey, N., Hemberger, D., ... Willis, P. (2020). GipsyX/RTGx, a new tool set for space geodetic operations and research. *Advances in Space Research*, *66*(3), 469–489. doi: 10.1016/j.asr.2020.04.015

Bills, B. G., Adams, K. D., & Wesnousky, S. G. (2007). Viscosity structure of the crust and upper mantle in western Nevada from isostatic rebound patterns of the late Pleistocene Lake Lahontan high shoreline. *Journal of Geophysical Research: Solid Earth*, *112*(B6). doi: 10.1029/2005JB003941

Blewitt, G. (2015). GPS and Space-Based Geodetic Methods. In *Treatise on Geo-*

physics (pp. 307–338). Elsevier. doi: 10.1016/B978-0-444-53802-4.00060-9

Blewitt, G., Hammond, W., & Kreemer, C. (2018). Harnessing the GPS Data Explosion for Interdisciplinary Science. *Eos*, *99*. doi: 10.1029/2018EO104623

Blewitt, G., Hammond, W. C., & Kreemer, C. (2009). Geodetic observation of contemporary deformation in the northern Walker Lane: 1. Semipermanent GPS strategy. In *Late Cenozoic Structure and Evolution of the Great Basin-Sierra Nevada Transition.* Geological Society of America. doi: 10.1130/2009.2447(01)

Blewitt, G., Kreemer, C., Hammond, W. C., & Gazeaux, J. (2016). MIDAS robust trend estimator for accurate GPS station velocities without step detection. *Journal of Geophysical Research: Solid Earth*(3), 2054–2068. doi: 10.1002/2015JB012552

Bock, Y., & Melgar, D. (2016). Physical applications of GPS geodesy: a review. *Reports on Progress in Physics*, *79*(10), 106801. doi: 10.1088/0034-4885/79/10/106801

Bormann, J. M., Hammond, W. C., Kreemer, C., & Blewitt, G. (2016). Accommodation of missing shear strain in the Central Walker Lane, western North America: Constraints from dense GPS measurements. *Earth and Planetary Science Letters*, *440*, 169–177. doi: 10.1016/j.epsl.2016.01.015

Bourne, S. J., England, P. C., & Parsons, B. (1998). The motion of crustal blocks driven by flow of the lower lithosphere and implications for slip rates of continental strike-slip faults. *Nature*, *391*(6668), 655–659. doi: 10.1038/35556

Briggs, R. W., Stephenson, W. J., McBride, J. H., Odum, J. K., Reitman, N. G., & Gold, R. D. (2021). Geophysical Constraints on the Crustal Architecture of the Transtensional Warm Springs Valley Fault Zone, Northern Walker Lane, Western Nevada, USA. *Journal of Geophysical Research: Solid Earth*, *126*(10), e2020JB020757. doi: 10.1029/2020JB020757

Cakir, Z., Ergintav, S., Akoğlu, A. M., Çakmak, R., Tatar, O., & Meghraoui, M. (2014). InSAR velocity field across the North Anatolian Fault (eastern Turkey): Implications for the loading and release of interseismic strain accumulation. *Journal of Geophysical Research: Solid Earth*, *119*(10), 7934–7943. doi: 10.1002/2014JB011360

Chaussard, E., Johnson, C. W., Fattahi, H., & Bürgmann, R. (2016). Potential and limits of InSAR to characterize interseismic deformation independently of GPS data: Application to the southern San Andreas Fault system. *Geochemistry, Geophysics, Geosystems*, *17*(3), 1214–1229. doi: 10.1002/2015GC006246

Chuang, R. Y., & Johnson, K. M. (2011). Reconciling geologic and geodetic model fault slip-rate discrepancies in Southern California: Consideration of nonsteady mantle flow and lower crustal fault creep. *Geology*, *39*(7), 627–630. doi: 10.1130/G32120.1

Chupik, C., Koehler, R., & Keen-Zebert, A. (2022). Complex Holocene Fault Ruptures on the Warm Springs Valley Fault in the Northern Walker Lane, Nevada–Northern California. *Bulletin of the Seismological Society of America*, *112*(1), 575–596. doi: 10.1785/0120200271

Community, U. (2006). *PBO GPS Network - P003-MohawkvallAZ2006 P.S., The GAGE Facility operated by EarthScope Consortium, GPS/GNSS Observations* [dataset]. The GAGE Facility operated by EarthScope Consortium. Retrieved from `https://doi.org/10.7283/T53776P8` doi: 10.7283/T53776P8

DeLano, K., Lee, J., Roper, R., & Calvert, A. (2019). Dextral, normal, and sinistral faulting across the eastern California shear zone–Mina deflection transition, California-Nevada, USA. *Geosphere*, *15*(4), 1206–1239. doi: 10.1130/GES01636.1

Dickinson, H., Freed, A. M., & Andronicos, C. (2016). Inference of the viscosity structure and mantle conditions beneath the Central Nevada Seismic Belt from combined postseismic and lake unloading studies. *Geochemistry, Geophysics,*

Geosystems, *17*(5), 1740–1757. doi: 10.1002/2015GC006207

Dixon, T. H., Miller, M., Farina, F., Wang, H., & Johnson, D. (2000). Present-day motion of the Sierra Nevada block and some tectonic implications for the Basin and Range province, North American Cordillera. *Tectonics*, *19*(1), 1–24. doi: 10.1029/1998TC001088

Dong, S., Ucarkus, G., Wesnousky, S. G., Maloney, J., Kent, G., Driscoll, N., & Baskin, R. (2014). Strike-slip faulting along the Wassuk Range of the northern Walker Lane, Nevada. *Geosphere*, *10*(1), 40–48. doi: 10.1130/GES00912.1

Eisses, A. K., Kell, A., Kent, G. M., Driscoll, N. W., LeRoy Baskin, R., Smith, K. D., ... Pullammanappallil, S. K. (2015). New constraints on fault architecture, slip rates, and strain partitioning beneath Pyramid Lake, Nevada. *Geosphere*, *11*(3), 683–704. doi: 10.1130/GES00821.1

Faulds, J. E., Henry, C. D., & Hinz, N. H. (2005). Kinematics of the northern Walker Lane: An incipient transform fault along the Pacific–North American plate boundary. *Geology*, *33*(6), 505. doi: 10.1130/G21274.1

Fay, N. P., & Humphreys, E. D. (2005). Fault slip rates, effects of elastic heterogeneity on geodetic data, and the strength of the lower crust in the Salton Trough region, southern California. *Journal of Geophysical Research: Solid Earth*, *110*(B9). doi: 10.1029/2004JB003548

Ford, H. A., Fischer, K. M., & Lekic, V. (2014). Localized shear in the deep lithosphere beneath the San Andreas fault system. *Geology*, *42*(4), 295–298. doi: 10.1130/G35128.1

Freed, A. M., Bürgmann, R., & Herring, T. (2007). Far-reaching transient motions after Mojave earthquakes require broad mantle flow beneath a strong crust. *Geophysical Research Letters*, *34*(19). doi: 10.1029/2007GL030959

Galehouse, J. S., & Lienkaemper, J. J. (2003). Inferences Drawn from Two Decades of Alinement Array Measurements of Creep on Faults in the San Francisco Bay Region. *Bulletin of the Seismological Society of America*, *93*(6), 2415–2433. doi: 10.1785/0120020226

Gold, R. D., Briggs, R. W., Crone, A. J., & DuRoss, C. B. (2017). Refining fault slip rates using multiple displaced terrace risers—An example from the Honey Lake fault, NE California, USA. *Earth and Planetary Science Letters*, *477*, 134–146. doi: 10.1016/j.epsl.2017.08.021

Gold, R. D., Briggs, R. W., Personius, S. F., Crone, A. J., Mahan, S. A., & Angster, S. J. (2014). Latest Quaternary paleoseismology and evidence of distributed dextral shear along the Mohawk Valley fault zone, northern Walker Lane, California. *Journal of Geophysical Research: Solid Earth*, *119*(6), 5014–5032. doi: 10.1002/2014JB010987

Gold, R. D., Stephenson, W. J., Odum, J. K., Briggs, R. W., Crone, A. J., & Angster, S. J. (2013). Concealed Quaternary strike-slip fault resolved with airborne lidar and seismic reflection: The Grizzly Valley fault system, northern Walker Lane, California. *Journal of Geophysical Research: Solid Earth*, *118*(7), 3753–3766. doi: 10.1002/jgrb.50238

Hammond, W. C., Blewitt, G., & Kreemer, C. (2011). Block modeling of crustal deformation of the northern Walker Lane and Basin and Range from GPS velocities. *Journal of Geophysical Research*, *116*(B4), B04402. doi: 10.1029/2010JB007817

Hammond, W. C., Kreemer, C., & Blewitt, G. (2009). Geodetic constraints on contemporary deformation in the northern Walker Lane: 3. Central Nevada seismic belt postseismic relaxation. In *Late Cenozoic Structure and Evolution of the Great Basin-Sierra Nevada Transition.* Geological Society of America. doi: 10.1130/2009.2447(03)

Hammond, W. C., & Thatcher, W. (2004). Contemporary tectonic deformation of the Basin and Range province, western United States: 10 years of observation with the Global Positioning System. *Journal of Geophysical Research: Solid*

Earth, *109*(B8). doi: 10.1029/2003JB002746

Hauge, T. A., Allmendinger, R. W., Caruso, C., Hauser, E. C., Klemperer, S. L., Opdyke, S., ... Oliver, J. (1987). Crustal structure of western Nevada from COCORP deep seismic-reflection data. *GSA Bulletin*, *98*(3), 320–329. doi: 10.1130/0016-7606(1987)98⟨320:CSOWNF⟩2.0.CO;2

Hill, E. M., & Blewitt, G. (2006). Testing for fault activity at Yucca Mountain, Nevada, using independent GPS results from the BARGEN network. *Geophysical Research Letters*, *33*(14), 2006GL026140. doi: 10.1029/2006GL026140

Hunter, J. D. (2007). Matplotlib: A 2d graphics environment. *Computing in Science & Engineering*, *9*(3), 90–95. doi: 10.1109/MCSE.2007.55

Hussain, E., Wright, T. J., Walters, R. J., Bekaert, D. P. S., Lloyd, R., & Hooper, A. (2018). Constant strain accumulation rate between major earthquakes on the North Anatolian Fault. *Nature Communications*, *9*(1), 1392. doi: 10.1038/s41467-018-03739-2

Kidder, S., Prior, D. J., Scott, J. M., Soleymani, H., & Shao, Y. (2021). Highly localized upper mantle deformation during plate boundary initiation near the Alpine fault, New Zealand. *Geology*, *49*(9), 1102–1106. doi: 10.1130/G48532.1

Kreemer, C., & Blewitt, G. (2021). Robust estimation of spatially varying common-mode components in GPS time-series. *Journal of Geodesy*, *95*(1), 13. doi: 10.1007/s00190-020-01466-5

Kreemer, C., Blewitt, G., & Hammond, W. C. (2009). Geodetic constraints on contemporary deformation in the northern Walker Lane: 2. Velocity and strain rate tensor analysis. In *Late Cenozoic Structure and Evolution of the Great Basin-Sierra Nevada Transition.* Geological Society of America. doi: 10.1130/2009.2447(02)

Kreemer, C., & Young, Z. M. (2022). Crustal strain rates in the Western United States and their relationship with earthquake rates. *Seismological research letters*, *93*(6), 2990–3008. doi: 10.1785/0220220153

Lamb, S., & Smith, E. (2013). The nature of the plate interface and driving force of interseismic deformation in the New Zealand plate-boundary zone, revealed by the continuous GPS velocity field. *Journal of Geophysical Research: Solid Earth*, *118*(6), 3160–3189. doi: 10.1002/jgrb.50221

Lowry, A. R., & Smith, R. B. (1994). Flexural rigidity of the Basin and Range-Colorado Plateau-Rocky Mountain transition from coherence analysis of gravity and topography. *Journal of Geophysical Research: Solid Earth*, *99*(B10), 20123–20140. doi: 10.1029/94JB00960

McCaffrey, R. (2005). Block kinematics of the Pacific–North America plate boundary in the southwestern United States from inversion of GPS, seismological, and geologic data. *Journal of Geophysical Research: Solid Earth*, *110*(B7). doi: 10.1029/2004JB003307

McKenzie, D., Nimmo, F., Jackson, J. A., Gans, P. B., & Miller, E. L. (2000). Characteristics and consequences of flow in the lower crust. *Journal of Geophysical Research: Solid Earth*, *105*(B5), 11029–11046. doi: 10.1029/1999JB900446

Meade, B. J., & Hager, B. H. (2005). Block models of crustal motion in southern California constrained by GPS measurements. *Journal of Geophysical Research: Solid Earth*, *110*(B3), 2004JB003209. doi: 10.1029/2004JB003209

Mongovin, D. D., & Philibosian, B. (2021). Creep on the Sargent Fault over the Past 50 Yr from Alignment Arrays with Implications for Slip Transfer between the Calaveras and San Andreas Faults, California. *Bulletin of the Seismological Society of America*, *111*(6), 3189–3203. doi: 10.1785/0120210041

Moore, M., England, P., & Parsons, B. (2002). Relation between surface velocity field and shear wave splitting in the South Island of New Zealand. *Journal of Geophysical Research: Solid Earth*, *107*(B9), ETG 5–1–ETG 5–7. doi: 10.1029/2000JB000093

Norris, R. J., & Cooper, A. F. (2003). Very high strains recorded in mylonites along the Alpine Fault, New Zealand: implications for the deep structure of plate boundary faults. *Journal of Structural Geology*, *25*(12), 2141–2157. doi: 10.1016/S0191-8141(03)00045-2

Norris, R. J., & Toy, V. G. (2014). Continental transforms: A view from the alpine fault. *Journal of Structural Geology*, *64*, 3–31. doi: 10.1016/j.jsg.2014.03.003

Nur, A., & Mavko, G. (1974). Postseismic Viscoelastic Rebound. *Science*, *183*(4121), 204–206. doi: 10.1126/science.183.4121.204

Pierce, I. K. D., Wesnousky, S. G., Owen, L. A., Bormann, J. M., Li, X., & Caffee, M. (2021). Accommodation of Plate Motion in an Incipient Strike-Slip System: The Central Walker Lane. *Tectonics*, *40*(2), e2019TC005612. doi: 10.1029/2019TC005612

Pollitz, F. F. (2001). Viscoelastic shear zone model of a strike-slip earthquake cycle. *Journal of Geophysical Research: Solid Earth*, *106*(B11), 26541–26560. doi: 10.1029/2001JB000342

Pollitz, F. F., McCrory, P., Svarc, J., & Murray, J. (2008). Dislocation models of interseismic deformation in the western United States. *Journal of Geophysical Research: Solid Earth*, *113*(B4). doi: 10.1029/2007JB005174

Prescott, W. H., Lisowski, M., & Savage, J. C. (1981). Geodetic measurement of crustal deformation on the San Andreas, Hayward, and Calaveras Faults near San Francisco, California. *Journal of Geophysical Research: Solid Earth*, *86*(B11), 10853–10869. doi: 10.1029/JB086iB11p10853

Prescott, W. H., & Nur, A. (1981). The accommodation of relative motion at depth on the San Andreas Fault System in California. *Journal of Geophysical Research: Solid Earth*, *86*(B2), 999–1004. doi: 10.1029/JB086iB02p00999

Ruhl, C. J., Abercrombie, R., Hatch, R., & Smith, K. (2020). *Relocated Earthquake Catalog - Seismogenic Depth Variation across the Transtensional Northern Walker Lane* [dataset]. Zenodo. doi: 10.5281/zenodo.4141085

Savage, J. C. (2000). Viscoelastic-coupling model for the earthquake cycle driven from below. *Journal of Geophysical Research: Solid Earth*, *105*(B11), 25525–25532. doi: 10.1029/2000JB900276

Savage, J. C., & Burford, R. O. (1973). Geodetic determination of relative plate motion in central California. *Journal of Geophysical Research*, *78*(5), 832–845. doi: 10.1029/JB078i005p00832

Savage, J. C., & Lisowski, M. (1998). Viscoelastic coupling model of the San Andreas Fault along the big bend, Southern California. *Journal of Geophysical Research*, *103*(B4), 7281–7292. doi: 10.1029/98JB00148

Savage, J. C., & Prescott, W. H. (1978). Asthenosphere readjustment and the earthquake cycle. *Journal of Geophysical Research: Solid Earth*, *83*(B7), 3369–3376. doi: 10.1029/JB083iB07p03369

Savage, J. C., Prescott, W. H., Chamberlain, J. F., Lisowski, M., & Mortensen, C. E. (1979). Geodetic tilt measurements along the San Andreas Fault in central California. *Bulletin of the Seismological Society of America*, *69*(6), 1965–1981. doi: 10.1785/BSSA0690061965

Sawyer, T. L., Briggs, R. W., & Ramelli, A. R. (2013). Paleoseismic investigation of the Mohawk Valley fault zone, Sierra County, northeastern California. *US Geological Survey Final Technical Report*, 1–33. doi: 10.1002/2014JB010987

Schmalzle, G., Dixon, T., Malservisi, R., & Govers, R. (2006). Strain accumulation across the Carrizo segment of the San Andreas Fault, California: Impact of laterally varying crustal properties. *Journal of Geophysical Research: Solid Earth*, *111*(B5). doi: 10.1029/2005JB003843

Surpless, B. (2008). Modern strain localization in the central Walker Lane, western United States: Implications for the evolution of intraplate deformation in transtensional settings. *Tectonophysics*, *457*(3-4), 239–253. doi: 10.1016/j.tecto.2008.07.001

Svarc, J. L., Savage, J. C., Prescott, W. H., & Ramelli, A. R. (2002). Strain accumulation and rotation in western Nevada, 1993–2000. *Journal of Geophysical Research: Solid Earth*, *107*(B5). doi: 10.1029/2001JB000579

Titus, S. J., Medaris, L. G., Wang, H. F., & Tikoff, B. (2007). Continuation of the San Andreas fault system into the upper mantle: Evidence from spinel peridotite xenoliths in the Coyote Lake basalt, central California. *Tectonophysics*, *429*(1), 1–20. doi: 10.1016/j.tecto.2006.07.004

Tong, X., Sandwell, D. T., & Smith-Konter, B. (2013). High-resolution interseismic velocity data along the San Andreas Fault from GPS and InSAR. *Journal of Geophysical Research: Solid Earth*, *118*(1), 369–389. doi: 10.1029/2012JB009442

Traoré, N., Le Pourhiet, L., Frelat, J., Rolandone, F., & Meyer, B. (2014). Does interseismic strain localization near strike-slip faults result from boundary conditions or rheological structure? *Geophysical Journal International*, *197*(1), 50–62. doi: 10.1093/gji/ggu011

Vauchez, A., Tommasi, A., & Mainprice, D. (2012). Faults (shear zones) in the Earth's mantle. *Tectonophysics*, *558-559*, 1–27. doi: 10.1016/j.tecto.2012.06.006

Vernant, P. (2015). What can we learn from 20 years of interseismic GPS measurements across strike-slip faults? *Tectonophysics*, *644-645*, 22–39. doi: 10.1016/j.tecto.2015.01.013

Wang, K., Zhu, Y., Nissen, E., & Shen, Z.-K. (2021). On the Relevance of Geodetic Deformation Rates to Earthquake Potential. *Geophysical Research Letters*, *48*(11), e2021GL093231. doi: 10.1029/2021GL093231

Wdowinski, S., Bock, Y., Baer, G., Prawirodirdjo, L., Bechor, N., Naaman, S., ... Melzer, Y. (2004). GPS measurements of current crustal movements along the Dead Sea Fault. *Journal of Geophysical Research: Solid Earth*, *109*(B5). doi: 10.1029/2003JB002640

Weiss, J. R., Walters, R. J., Morishita, Y., Wright, T. J., Lazecky, M., Wang, H., ... Parsons, B. (2020). High-Resolution Surface Velocities and Strain for Anatolia From Sentinel-1 InSAR and GNSS Data. *Geophysical Research Letters*, *47*(17), e2020GL087376. doi: 10.1029/2020GL087376

Wesnousky, S. G. (2005a). Active faulting in the Walker Lane. *Tectonics*, *24*(3). doi: 10.1029/2004TC001645

Wesnousky, S. G. (2005b). The San Andreas and Walker Lane fault systems, western North America: transpression, transtension, cumulative slip and the structural evolution of a major transform plate boundary. *Journal of Structural Geology*, *27*(8), 1505–1512. doi: 10.1016/j.jsg.2005.01.015

Wesnousky, S. G., Bormann, J. M., Kreemer, C., Hammond, W. C., & Brune, J. N. (2012). Neotectonics, geodesy, and seismic hazard in the northern Walker Lane of western North America; thirty kilometers of crustal shear and no strike-slip? *Earth and planetary science letters*, *329-330*, 133–140. doi: 10.1016/j.epsl.2012.02.018

Wessel, P., Luis, J. F., Uieda, L., Scharroo, R., Wobbe, F., Smith, W. H. F., & Tian, D. (2019). The generic mapping tools version 6. *Geochemistry, Geophysics, Geosystems*, *20*, 5556–5564. doi: doi.org/10.1029/2019GC008515

Wills, C. J., & Borchardt, G. (1993). Holocene slip rate and earthquake recurrence on the Honey Lake fault zone, northeastern California. *Geology (Boulder)*, *21*(9), 853–856. doi: 10.1130/0091-7613(1993)021⟨0853:HSRAER⟩2.3.CO;2

Wright, T., Parsons, B., & Fielding, E. (2001). Measurement of interseismic strain accumulation across the North Anatolian Fault by satellite radar interferometry. *Geophysical Research Letters*, *28*(10), 2117–2120. doi: 10.1029/2000GL012850

Zhu, L. (2000). Crustal structure across the San Andreas Fault, southern California

from teleseismic converted waves. *Earth and Planetary Science Letters*, *179*(1), 183–190. doi: 10.1016/S0012-821X(00)00101-1

Zhu, Y., Wang, K., & He, J. (2020). Effects of earthquake recurrence on localization of interseismic deformation around locked strike-slip faults. *Journal of geophysical research. Solid earth*, *125*(8), n/a. doi: 10.1029/2020JB019817

Zuza, A. V., & Cao, W. (2020). Seismogenic thickness of California: Implications for thermal structure and seismic hazard. *Tectonophysics*, *782-783*, 228426. doi: 10.1016/j.tecto.2020.228426